Journal of Catalysis 341 (2016) 104–115

Contents lists available at ScienceDirect

Journal of Catalysis

journal homepage: www.elsevier.com/locate/jcat

Comparative study of the catalytic thermodynamic barriers for two homologous Mn- and Fe-non-heme oxidation catalysts

M. Papastergiou [a], P. Stathi [a], E.R. Milaeva [b], Y. Deligiannakis [c,*], M. Louloudi [a,*]

[a] Laboratory of Inorganic Chemistry, Department of Chemistry, University of Ioannina, 45110 Ioannina, Greece
[b] Department of Medicinal Chemistry and Fine Organic Synthesis, Lomonosov Moscow State University 119991, Russia
[c] Laboratory of Physical Chemistry of Materials & Environment, Department of Physics, University of Ioannina, 45110 Ioannina, Greece

ARTICLE INFO

Article history:
Received 12 May 2016
Revised 23 June 2016
Accepted 23 June 2016

Keywords:
Catalytic epoxidation
Mn- and Fe-non-heme catalysts
H_2O_2 activation
EPR
Thermodynamics
Low-T UV–vis

ABSTRACT

Two sets of homologous Mn- and Fe-catalysts, [$Mn^{II}LCl_2$], [$Fe^{II}LCl_2$] and [$Mn^{II}L(OAc)_2$], [$Fe^{II}L(OAc)_2$] have been synthesized. A detailed comparative study of their catalytic oxidative performance with H_2O_2, *in tandem* with EPR and Low-Temperature UV–vis spectroscopies has been carried out. The [Metal-L$(OAc)_2$] and [Metal-LCl_2] catalysts did not show any difference in their catalytic behavior i.e. there is no effect of the labile ligands on the studied catalysis. It is found that the Mn-catalysts consistently outcompeted the homologous Fe-catalysts i.e. TOFs (Mn) = 162 *vs.* TOFs (Fe) = 16. We found that the Fe-catalyst faces a significantly higher activation barrier than the Mn-catalyst i.e. $E_a(\mathbf{Fe^{II}L}(OAC)_2)$ = 91KJ/mol $\gg E_a(\mathbf{Mn^{II}L}(OAC)_2)$ = 55 kJ/mole, while the free-energy difference, $\Delta G(\mathbf{Fe^{II}L}(OAC)_2) \sim \Delta G(\mathbf{Mn^{II}L}(OAC)_2) \sim -145$ kJ/mole, did not make difference. Taken altogether the present data clarify that the main thermodynamic barrier, ultimately determining the overall catalytic performance, of these homologous Mn- and Fe-catalysts is the activation energy for the transient intermediates i.e. Mn^{II} to Mn^{IV}=O for the Mn-catalysts and Fe^{II} to Fe^{III}—OOH for the Fe-catalysts. A unified/consistent catalytic thermodymanic concept is discussed, that bears relevance to the catalytic behavior of many non-heme Mn- *vs.* Fe-oxidation catalysts.

1. Introduction

In fine chemicals technology, among the end-targets of applied oxidation catalysis is to produce more efficient catalysts *in tandem* with less expensive and more environmentally acceptable processes [1]. Epoxidation reactions of olefins constitute an industrially applicable process for production of epoxides i.e. widely used as raw materials or intermediates for epoxy resin production, paints, surfactants and medicines [2,3]. Environmental regulations on industrial production of chemicals, force companies to diminish environmental pollution [4–7]. Within this environmental/economic context, the use of manganese and iron complexes as active catalysts, associated with hydrogen peroxide as the primary oxidant, is highly desirable. H_2O_2 is increasingly used as oxidant both in industry and in academic research, since its only by-product is water. In the same context, non-heme manganese and non-heme iron catalysts present advantages e.g. convenient synthesis, low production-cost, considerable stability, selectivity toward formation of epoxides [1,8].

In general, the stability and selectivity of a homogeneous catalyst are strongly related to its molecular structure. Consideration of steric, electronic and conformational properties is necessary i.e. in order to design appropriate ligands for metal complexes which will serve as efficient catalysts. Among other properties, the ligands must [i] be resilient to oxidation, and [ii] strongly electron donating, in order to achieve high oxidation states of the active metal [1]. In this context, polydentate ligands containing 2-pyridylmethyl or 2-pyridyl fragments attached to a tertiary nitrogen atom, contain both σ-donor and π-acceptor binding sites. Thus, ligands of this class (e.g. such as tris (2-pyridylmethyl) amine, *tpa* or N,N,N′,N′-tetrakis (2-pyridylmethyl) ethylenediamine, *tpen*) are capable of stabilizing both high- and low-oxidation states in their metal complexes [9–11]. Moreover, ligands containing 2,6-di-*tert*-butyl-4-hydroxyphenol groups on the periphery of the ligand frame are also interesting because they might provide antioxidant features [12] and additional endurance to metal oxidation catalysts. 2,6-di-*tert*-butyl-4-hydroxyphenol has been already used as substituent on the porphyrin ring offering remarkable performance in oxidations catalyzed by metalloporphyrins [13–18]. Recently, a new series of non-heme metal complexes with di-(2-picolyl) amine ligand bearing this 2,6-di-*tert*-butyl-4-hydroxyphenol

* Corresponding authors.

http://dx.doi.org/10.1016/j.jcat.2016.06.017
0021-9517/

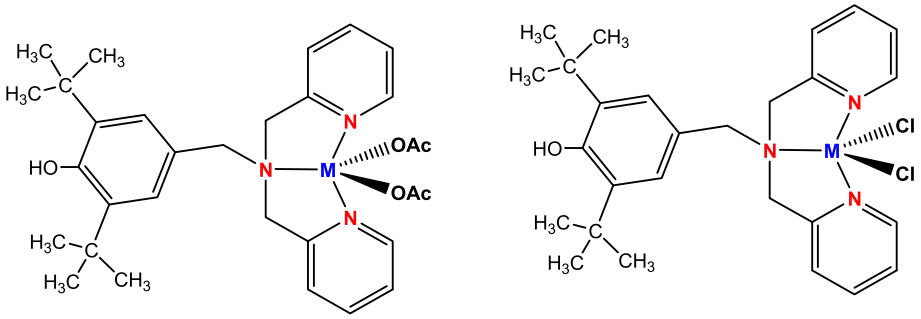

Fig. 1. Structures of $[Mn^{II}L(OAc)_2]$ (**1**), $[Mn^{II}LCl_2]$ (**2**), $[Fe^{II}L(OAc)_2]$ (**3**) and $[Fe^{II}LCl_2]$ (**4**) complexes.

moiety has been reported by one of us [19]. Herein, manganese and iron complexes containing the [N-(3,5-Di-*tert*-butyl-4-hydroxybenzyl)-N,N-di-(2-pyridylmethyl)]amine (L) ligand [19] (Fig. 1) have been evaluated as homogeneous catalysts for alkene epoxidation with hydrogen peroxide.

Herein, we present a method where low-temperature UV–vis spectroscopy was used *in tandem* with low-temperature Electron Paramagnetic Resonance (EPR) to study the transient redox/catalytic intermediates formed during the catalytic cycle of the $[Mn^{II}LX_2]$ and $[Fe^{II}LX_2]$ complexes. EPR is eminently suited for quantitative monitoring of Fe^{III} and Mn^{II} states [20]. Transient oxidation states e.g. ($Fe^{III}O$—O), Fe^{V}, Mn^{III}, (Mn^{IV}=O) can also be detected by EPR [20–22]; however, under ambient temperature, their population is usually rapidly evolving. Therefore they can be trapped only by a systematic freeze-quench protocol that eventually allows optimal detection of these elusive species by EPR. Previously, we have reported the detection of such a catalytic intermediate Fe^{IV} state in a SiO_2-[Fe-porphyrin] system [15]. In that system, the Fe^{IV}-oxo center was shown to be magnetically coupled with a porphyrin radical i.e. forming the highly-reactive ferryl-species that determines the catalytic performance [15]. In the case of Mn-catalysts, the evolution to higher oxidation states, generated via oxidation of an initial Mn^{III} state has been reported [23] and EPR detection of Mn^{IV} in Mn(salen) complexes has been also demonstrated [23]. In the aforementioned work [23] the Mn^{IV} state could not been trapped during a 'standard' catalytic run; instead, a Mn^{IV} species, was formed by reaction of the initial Mn^{V}-oxo intermediate with the solvent in the absence of a substrate.

Apart from the detection of the elusive transient intermediates, their thermodynamic parameters i.e. activation energy, entropy, enthalpy, Gibbs free energy, are important. Moreover, a direct comparative study of the catalytic and thermodynamic parameters of homologous non-heme Fe and Mn complexes should provide profound insights into the catalytic mechanisms and energetics. Recently, systematic differences have been documented in the catalytic behavior of homologous Mn- *vs.* Fe-complexes [24–26], however a thermodynamic basis of these observations is still in need. In this context, herein we present the first comparative catalytic/thermodynamic study of the homologous complexes $[Mn^{II}L(OAc)_2]$ (**1**) *vs.* $[Fe^{II}L(OAc)_2]$ (**3**) and $[Mn^{II}LCl_2]$ (**2**) *vs.* $[Fe^{II}LCl_2]$ (**4**). A systematic freeze-quench EPR study was carried out to trap the transient intermediates and then to monitor the full time-course of their evolution. In parallel we have performed detailed kinetic studies of the redox evolution of monitoring their UV–vis spectra at a range of temperatures from +25 °C to −45 °C. Low-Temperature UV–vis (LT-UV–vis) spectroscopy allows a *continuous* mapping of the spectral evolution of the complexes. Then, a thermodynamic analysis of the LT-UV–vis data allowed numerical estimates of the activation energies, E_a, as well as $\Delta S^{\ddagger}$, $\Delta H^{\ddagger}$, $\Delta G^{\ddagger}$ for the Fe- and Mn-complexes. Based on the EPR and thermodynamic data, we construct a reaction-path scheme which unravels that the transient intermediates of the Fe-catalysts have higher E_a than the homologous Mn-catalysts, and as result Fe-catalysts have lower catalytic performance than the Mn-catalysts.

2. Materials and methods

2.1. Materials

All synthetic works were carried out under ambient air and at room temperature (25 °C). All solvents were purchased from Aldrich and used as received. The following chemical substrates were obtained in their highest commercial purity, stored at 5 °C and purified by passing through a column of basic alumina prior to use (Aldrich): Cyclohexene, Cyclooctene, Limonene, 1-hexene, cis-stilbene, styrene, trans-β-methylstyrene. Hydrogen peroxide was 30% (w/w) aqueous solution. GC analysis was performed using an 8000 Fisons chromatograph with a Flame Ionization Detector or a Shimadzu GC-17A gas chromatograph coupled with a GC-MS-QP5000 mass spectrometer. Continuous-flow of H_2O_2 was provided by a digitally-controlled syringe pump (SP101IZ WPI). Solution potential E_h was measured *in situ* by a Metrohm platinum redox electrode (type 6.0401.100).

2.2. Catalytic procedure

In the reactions catalyzed by Mn-complexes **1** and **2**, H_2O_2 was slowly added, over a total time of 30 min, in an acetone/MeOH (450/200 μl) solvent mixture under ambient air, at room temperature (25 °C). Then, the alkene (1 mmol), ammonium acetate (1 mmol) as cocatalytic additive, and manganese-catalyst (1 μmol) were added and the resulting reaction solution was vigorously stirred in a glass round-bottom flask for 6 h under ambient conditions. We underline that ammonium acetate is added as an additive that is absolutely required in order to generate efficient Mn-catalytic systems [27]. Acetophenone or bromobenzene was used as internal GC standards. The molar ratio of [Mn-catalyst:H_2O_2:CH_3COONH_4:substrate] was equal to [1:2000:1000:1000 μmol]. The total volume of catalytic reaction was about 1 ml.

In the reactions catalyzed by Fe-complexes **3** and **4**, H_2O_2 diluted in CH_3CN solvent (1:10 v/v) was slowly added (within a period of 5 min) to a CH_3CN solution containing the catalyst (1 μmol) and the substrate (1000 μmol) under N_2 atmosphere at room temperature (25 °C). The molar ratio [Fe-catalyst:H_2O_2:substrate] was equal to [1:500:1000 μmol]. Acetophenone or bromobenzene was used as internal GC standards. The total volume of catalytic reaction was approximately 1 ml.

The progress of the catalytic reactions was monitored by GC-MS for 20 μl samples, periodically taken from the reaction mixture. Quantitative analysis of the GC data was done by comparing the integrals of the GC peaks *vs.* the internal standard, thus providing the substrate conversion and product yield. Reactions were

completed within 6 h for Mn-catalysts and within 24 h for Fe-catalysts. Error-bars indicated in the data were derived from at least three replicates of each experiment.

Turnover Numbers and Turnover Frequencies Calculations

TONs were calculated using Eq. (1a)

$$\text{TONs} = \frac{\text{moles of product}}{\text{moles of catalyst}} \quad (1a)$$

TOFs were calculated using Eq. (1b)

$$\text{TOFs} = \frac{\text{TONs}}{t} \quad (1b)$$

2.3. Low temperature UV–vis spectroscopy

Low-temperature UV–vis spectra were recorded in a Hitachi spectrophotometer operating in the 190–900 nm wavelength range, in 3 ml quartz cuvettes (1 cm optical path). The sample was cooled in a Unisoku cryostat that was inserted inside the UV–vis spectrophotometer beam-chamber. This system allows digital control of sample-temperature from +100 °C down to −100 °C. Cooling of the sample was achieved by a controlled-flow of cold N_2-gas derived from heating of liquid-N_2. This allows temperature stabilization with an error of ±0.1 °C.

UV–vis sample preparation: For the low-temperature UV–vis study of the catalytic reaction, the metal-complex was solubilized to the suitable solvent i.e. CH_3CN for the Fe-complex or acetone/MeOH mixture in the case of Mn-complex; the solution cuvette was inserted to the cryostat, cooled to the desired temperature and allowed to equilibrate for 10 min, under stirring. Then, the substrate plus co-catalyst, when Mn-catalysts were used, plus H_2O_2 was added at this time-point ($t = 0$) and the collection of the UV–vis spectra (240–900 nm) was started, with a [1 spectrum/min] rate.

2.4. EPR spectroscopy

Electron paramagnetic resonance (EPR) spectra were recorded at liquid N_2 temperature 77 K with a Bruker ER200D spectrometer equipped with an Agilent 5310A frequency counter. The spectrometer was running under home-made software based on Lab View.

EPR sample preparation: all EPR samples were prepared in 5 mm internal diameter quartz tubes by Wilmad Glass. In the case of the Mn-complexes, appropriate amounts of the catalytic reaction components were dissolved in acetone/methanol mixture with a molar ratio [catalyst]: $[H_2O_2]$:$[CH_3COONH_4]$:[cyclohexene] = [1:2000:1000:1000 μmol]. For the study of Fe-catalysts, CH_3CN was used as solvent containing a molar ratio of [catalyst]:$[H_2O_2]$:[cyclohexene] = [1:500:1000 μmol].

Time-evolution of the EPR spectra: When all catalytic components were added into the EPR tube, this was immediately i.e. within 5 s, frozen at 77 K. The EPR spectrum of this sample is referred as "t_0". To record the time-evolution of the EPR spectra, the sample was thawed at room temperature and allowed to evolve for a predetermined time interval, followed by rapid freezing at 77 K, within 5 s. Numerical simulation of experimental EPR spectra was performed with Easy Spin 4.5.1 [28] software.

3. Results

3.1. Catalytic performance evaluation

Mn-catalysts: Table 1 lists the results of catalytic data obtained for the Mn^{II}- and Fe^{II}-complexes. Based on these, we observe that both non-heme Mn^{II} complexes **1** and **2** are efficient in alkene oxidations providing significant yields (39–97%), and high selectivity for epoxide products (the mass balance is 99 ± 1%) in most of the cases. In order to generate efficient catalytic systems, ammonium acetate was added as additive. As reported many times previously [29–31], CH_3COONH_4 plays a multiple role in Mn^{II}/H_2O_2 and this can attributed to a dual acid-base role for CH_3COONH_4 able to act as proton-donor and proton-acceptor [29–31]. More precisely, according to the catalytic mechanism we have proposed recently [i] CH_3COO^- abstracts a proton from H_2O_2, promoting its coordination to Mn^{II} and formation of Mn^{II}—OOH species and [ii] subsequently, NH_4^+, by acting as a proton donor to Mn^{II}—OOH, accelerates heterolytic O—O cleavage forming the active Mn^{IV}=O species which [iii] catalyzes alkene epoxidation [27]. Oxidation of cyclooctene and hexene-1 catalyzed by **1** and **2** provided 100% selectivity for *cis*-epoxide with 54.0–64.0% and 10.3–10.5% yield, and 100% m.b. respectively (Fig. 2). The total cyclohexene oxidation yield was 67.2% for **1** and 57.0% for **2**. In particular, both **1** and **2** provided mainly epoxide with 61.4–53.3% yields, while the allylic oxidation path resulted in small amounts of 2-cyclohexen-1-ol (3.6–2.1%) and 2-cyclohexen-1-one (2.2–1.7%). During the epoxidation of styrene and *cis*-stilbene by **1** and **2**, the corresponding epoxide was the only product, *cis*-stilbene-epoxide in the case of *cis*-stilbene, with yields 39.0–42.3% and 44.0–43.7% respectively. The methyl-substituted derivative of styrene, trans-β-methyl styrene, is more reactive than styrene giving total oxidation yields of 97.3% and 66.5% catalyzed by **1** and **2** respectively; in both cases, the corresponding *trans*-epoxide was identified as single product. The products detected from limonene oxidation were as follows: (i) two epoxides (*cis* and *trans*) originated from epoxidation of the electron-rich double bond in the 1,2-position and (ii) alcohols derived from hydroxylation either at the 1-position or at the 6-position. The total yield of the oxidation products was raised at 86.1% catalyzed by Mn-catalyst **1** and 60.6% by **2**. Noticeably, the $[Mn^{II}L(OAc)_2]$ and $[Mn^{II}LCl_2]$ catalysts did not show any remarkable difference in their catalytic behavior i.e. there is no detectable effect of the labile ligands on the studied catalysis.

Fe-catalysts: The catalytic evaluation of the Fe^{II}-complexes **3**, **4** with H_2O_2, generally showed consistently much lower catalytic efficiency than the corresponding Mn^{II}-complexes **1**, **2**. Analogous trend was reported for the catalytic performance of other homologous Fe-non-heme *vs.* Mn-oxidation catalysts [24]. Here, in oxidation reactions of alkenes the Fe-catalysts provide varying yields (1.4–78.9%) (Fig. 3). We underline however the remarkable turnover numbers (see Table 1), achieved by the present Fe-non-heme catalysts **3** and **4** approaching 394 TONs i.e. compared with analogous non-heme Fe-catalysts in Fig. 4A.

The total cyclohexene oxidation yield was 26.4% with 132 TONs for **3,** and 19.5% with 97 TONs for **4**. Allylic oxidation formed 2-cyclohexen-1-*ol* (9.8–8.0%) and 2-cyclohexen-1-*one* (13.4–8.9%). However cyclohexene epoxidation was also observed, with low epoxide yields (3.1–2.7%). Oxidation of cyclooctene provides 100% selectivity for *cis*-cyclooctene epoxide with 19.5% and 16.5% yield and 97 and 82 TONs, by **3** and **4** respectively. Hexene-1 that is a rather hard oxidation substrate showed epoxide yields from 1.4% to 3.0% by **3** and **4** respectively and 100% selectivity for the *cis*-epoxide.

The products detected from limonene oxidation, were two epoxides (*cis* and *trans*) originating from epoxidation of the electron-rich double bond in the 1,2-position and alcohols derived from hydroxylation in 1-, 2- and 6-position of the limonene ring. Additionally, considerable amounts of the corresponding ketone at 6-position were also formed (see details in Table 1). Oxidation products from the more accessible, but less electron-rich 8, 9-double-bond were not observed. The total yield of the limonene oxidation products raised at 25.7% with 128 TONs for $Fe^{II}L(OAc)_2$ and 29.3% with 146 TONs for $Fe^{II}LCl_2$.

Table 1
Hydrocarbon oxidation catalyzed by **$Mn^{II}L(OAc)_2$**, **$Mn^{II}LCl_2$**, **$Fe^{II}L(OAc)_2$** and **$Fe^{II}LCl_2$** with H_2O_2.

Substrate	Product	$LMn(OAc)_2$[a]			$LMnCl_2$[a]			$LFe(OAc)_2$[b]			$LFeCl_2$[b]		
		Yield (%)[a]	TON[c]	TOF[d]	Yield (%)[a]	TON[c]	TOF[d]	Yield (%)[b]	TON[c]	TOF[d]	Yield (%)[b]	TON[c]	TOF[d]
Cyclohexene	cis-Epoxide	61.4			53.3			3.1			2.66		
	2-Cyclohexenone	2.2			1.7			13.4			8.87		
	2-Cyclohexenol	3.6			2.1			9.8			7.96		
			672	112		570	95		132	5		97	4
Cyclooctene	cis-Epoxide	54.0	540	90	64.0	640	107	19.5	97	4	16.5	82	3
Limonene	Epoxide	66.0			47.7			12.5			13.4		
	Limonene alcohol												
	Limonene ketone	20.1			12.9			7.2			9.5		
								6.0			6.4		
			861	143		606	101		128	5		146	6
Hexene-1	cis-Epoxide	10.3	103	17	10.5	105	17	1.4	7	0.3	3.0	15	0.6
cis-stilbene	cis-Epoxide	44.0			43.7			36.0			14.6		
	Benzaldehyde							20.1			30.0		
			440	73		437	73		280	11		223	9
Styrene	Epoxide	39.0			42.3			5.4			15.01		
	Benzaldehyde							41.7			44.3		
			390	65		423	70		235	9		296	12
Trans-β-methylstyrene	trans-Epoxide	97.3			66.5			16.7			48.25		
	Benzaldehyde							61.2			30.54		
			973	162		665	111		390	16		394	16

[a] Conditions ratio of catalyst:H_2O_2:CH_3COONH_4:substrate = 1:2000:1000:1000; Equivalent of catalyst = 1 μmol in 0,65 ml CH_3COOCH_3:CH_3OH (0,45:0,20); The reactions were completed within 6 h.
[b] Conditions ratio of catalyst:H_2O_2:substrate = 1:500:1000; equivalent of catalyst = 1 μmol in 0.9 ml MeCN; the reactions were completed within 24 h.
[c] TON: turnover number, moles of epoxide formed per mole of catalyst.
[d] TOF: turnover frequency which is calculated by the expression [epoxide]/[catalyst] ∗ time (h^1).

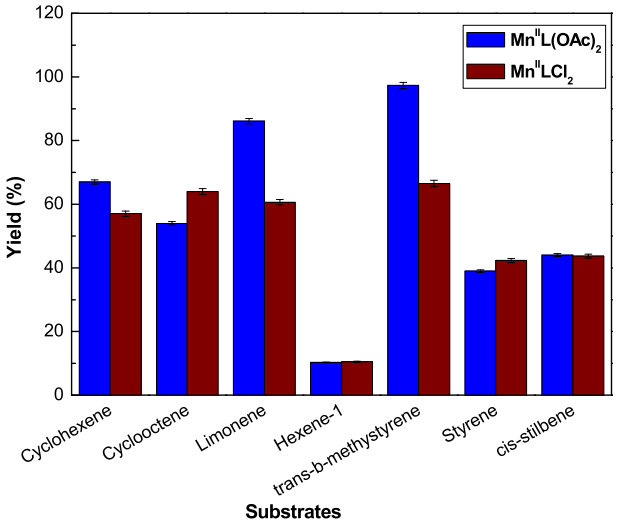

Fig. 2. Bar chart representation of alkene epoxidations catalyzed by Mn^{II} complexes **1** and **2** in the presence of H_2O_2. See Table 1 for further details.

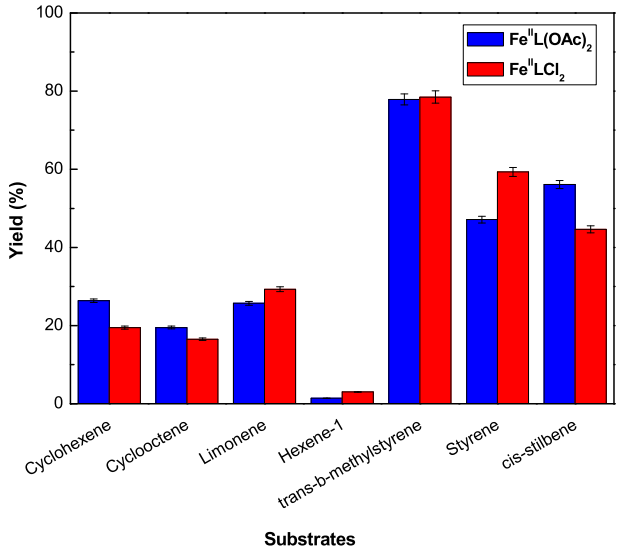

Fig. 3. Bar chart representation of alkene epoxidations catalyzed by Fe^{II} complexes **3** and **4** in the presence of H_2O_2. See Table 1 for further details.

Cis-stilbene was oxidized by **3** and **4** with total oxidation yields of 56.1% (280 TONs) and 44.6% (223 TONs) respectively. The products were identified as *cis*-epoxide and benzaldehyde. Styrene oxidation provided benzaldehyde as major product generated from oxidative cleavage of the exo-cyclic double bond. However, epoxide has been also formed by direct oxidation of the same double bond. Overall, styrene was oxidized by **3** and **4** with total oxidation yields of 47.1–59.3% and 235, 296 TONs respectively. *Trans*-β-methylstyrene oxidation by **3** provided benzaldehyde, as major product (61.2%). *Trans*-epoxide has been also detected (16.7%). On the contrary, oxidation of *trans*-β-methylstyrene by **4** provided trans-epoxide as major product (48.2%) and, at the same time, considerable amount of benzaldehyde has been also observed (30.5%). Overall, *trans*-β-methyl-styrene was oxidized by **3** and **4** with total oxidation yields of 77.9–78.7% and 390–394 TONs respectively.

The Fe catalysts **3** and **4** show no difference in their catalytic behavior, thus -as in the case of the Mn-catalysts **1** and **2** -their labile ligands i.e., chloride and acetate play no role in the catalysis studied herein (present data, see Table 1).

For comparison, we notice that the present homogeneous Fe-catalysts show remarkably higher turnover numbers (up to 390) (see Table 1, Fig. 4A) compared with other non-heme Fe-catalysts i.e. $DPEIFe^{III}Cl$ [24] and $FeCl_2(btaH)^2$ [32] studied previously by us under the same catalytic conditions, which provided TONs close to 46 (Fig. 4A); the enhanced catalytic activity of the present

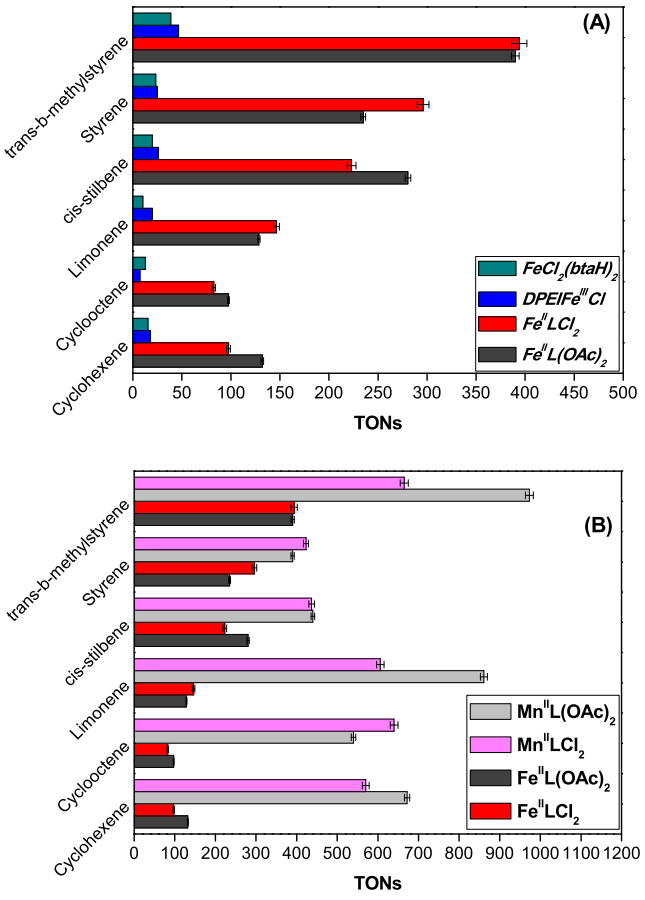

Fig. 4. (A) Total turnover numbers for alkene epoxidations with H_2O_2 catalyzed by **$Fe^{II}L(OAc)_2$**, **$Fe^{II}LCl_2$**, compared with other non-heme Fe catalysts DPEIFe^{III}Cl and $FeCl_3(btaH)_2$ and (B) comparison of TONs achieved by **$Mn^{II}(OAc)_2$**, **$MnLCl_2$** vs. **$Fe^{II}L(OAc)_2$** and **$Fe^{II}LCl_2$**.

Fe-complexes **3** and **4** is assigned to the different coordination and geometrical environments around the Fe-centers.

A comparison of the catalytic TONs of the present Fe-catalysts **3** and **4** *vs.* the homologous Mn-catalysts **1** and **2** (Fig. 4B), reveals that Mn-catalysts show consistently remarkable higher turnover numbers (TONs) than the homologous Fe-catalysts. As we show hereafter, redox/thermodynamics of the higher oxidation states determine this phenomenon.

Catalytic Kinetics, TOFs: [A] Mn-catalyst: the time-course profiles of the $Mn^{II}L(OAc)_2$- and $Mn^{II}LCl_2$-catalyzed oxidations of cyclohexene in conjunction with the observed solution potential of E_h (*vs.* standard hydrogen electrode, SHE) are presented in Fig. 5. At the beginning of the reaction catalyzed by $Mn^{II}L(OAc)_2$, E_h was +425 mV; after 3 h it dropped to +305 mV with a 50% epoxidation yield and finally after 6 h reaction time, it approached a steady value of E_h = +296 mV with a yield of 67.2%. In the case of $Mn^{II}LCl_2$-catalyzed epoxidation, at t = 0 h, E_h was +337 mV and then decreased to +283 mV (t = 2 h), providing a product yield of 48.0%; at t = 6 h, E_h approached +270 mV with 57.4% epoxidation yield. Similar time course profiles of the homogeneous catalysts have been observed for all substrates used herein demonstrating that the oxidation reactions are completed within 6 h. Based on this finding the Turnover Frequencies (TOFs) listed in Table 1 have been calculated. Moreover, the very good correlation of the [E_h *vs.*% yield] data in Fig. 5 shows that the catalytic reactions proceed *in tandem* with consumption of oxidative equivalents, as we show hereafter by EPR- via formation of the transient Mn^{IV}=O states.

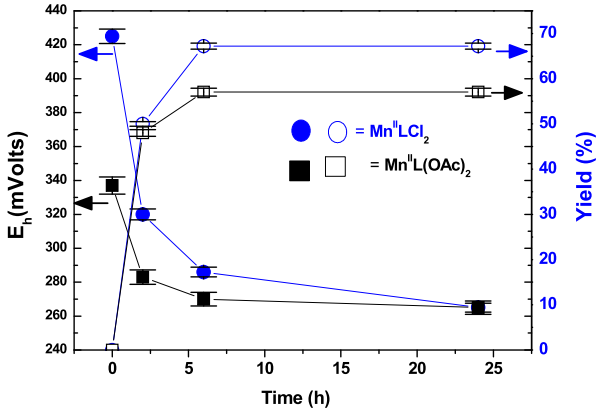

Fig. 5. Time dependence of cyclohexene epoxidation and solution redox potential for the same reaction catalyzed by **$Mn^{II}L(OAc)_2$** and **$Mn^{II}LCl_2$**.

[B] Fe-catalysts: The time-course profiles of the $Fe^{II}L(OAc)_2$- and $Fe^{II}LCl_2$-catalyzed oxidations of cyclooctene in conjunction with the observed redox potential of solution E_h are presented in Fig. 6. At the beginning of the reaction catalyzed by $Fe^{II}L(OAc)_2$, E_h was +475 mV; after 12 h it dropped to +450 mV with a 8.8% epoxidation yield and finally after a reaction time of 24 h, it approached a value of E_h = +430 mV with a 19.5% yield. In the case of $Fe^{II}LCl_2$ catalyzed epoxidation, at reaction time t = 0 h, E_h was +490 mV and then decreased to +460 mV (t = 12 h), providing a product yield of 5.0% and at t = 24 h, E_h approached +441 mV with 16.5% epoxidation yield. Similar time course profiles of the homogeneous catalysts have been observed for all substrates used herein. The Turnover Frequencies (TOFs) listed in Table 1 have been calculated on the basis that the Fe-depended oxidations were completed within 24 h.

Thus, the data in Figs. 5 and 6 and the TONs, TOFs in Table 1 reveal an important difference between the Fe-catalysts **3** and **4** *vs.* the Mn-catalysts **1** and **2**.

$$\text{TONs, TOFs[Mn-systems]} \gg \text{TONs, TOFs[Fe-systems]}$$

The Mn catalysts have TOFs in the range of 100 that are about × 20-fold higher than the TOFs (~5) of the Fe-catalysts. Mn catalysts cycle × 20-times more rapidly and consume much more H_2O_2 equivalents than the homologous Fe-catalysts.

This striking difference has been observed previously for homologous Mn, Fe non-heme catalysts [24–26] i.e. typically for the same ligand, Mn-catalysts show higher TONs than the Fe-catalysts, however a direct thermodynamic explanation has not

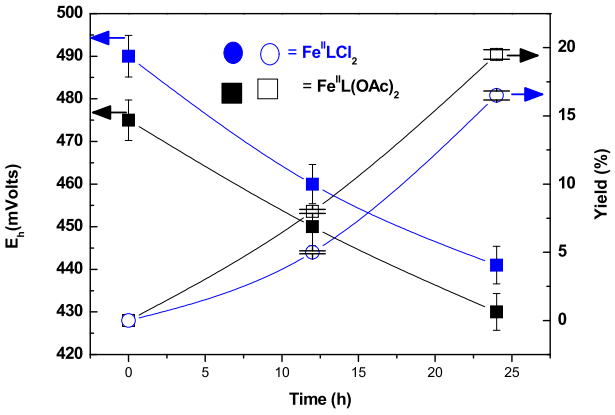

Fig. 6. Time dependence of cyclohexene epoxidation and solution redox potential for the same reaction catalyzed by **$Fe^{II}L(OAc)_2$** and **$Fe^{II}LCl_2$**.

been attempted so far. To do this, in principle, we have to consider the rate-limiting steps that may be involved in such reactions: in oxidative catalysis both Mn- and Fe-complexes usually advance *via* high oxidation states i.e. Fe^{IV} [33] and Mn^{IV} [34,35]. The redox potential of the couples Fe^{2+}-Fe^{3+}/Fe^{4+} is higher than the couple Mn^{2+}/Mn^{4+} i.e. for this reason mild oxidants could suffice to activate Mn-complexes while stronger ones are necessary for Fe-complex activation. Herein, quantitative insight into these trends was achieved by *in situ* monitoring of the oxidative evolution of the Fe- and Mn-catalysts, using low-temperature UV–vis and freeze-quench EPR spectroscopies.

3.2. Mechanistic spectroscopic studies

3.2.1. EPR spectroscopy

$Mn^{II}L(OAC)_2$: Fig. 7 shows 77 K EPR spectra for $Mn^{II}L(OAC)_2$ in acetone/methanol. The spectra are typical for a mononuclear Mn^{II} ($S = 5/2$, $I = 5/2$) [20]. After addition of H_2O_2 and ammonium acetate, the Mn^{II} signal intensity decreased gradually, and a new broad signal with effective values in ~5.5 and ~3.0–3.5 was detected. This new signal was maximized within 20 min, see inset Fig. 7C, and then decayed again. The oxidative evolution of this signal indicates that originates from high Mn oxidation states. Taking into account literature EPR data for Mn^{IV} (salen) [21,22,36] this EPR signal can be assigned to a monomeric Mn^{IV} ($S = 3/2$) spin system.

Numerical calculations of EPR spectra for Mn^{II} ($S = 5/2$, $I = 5/2$) and Mn^{IV} ($S = 3/2$, $I = 5/2$) were performed using the spin Hamiltonian

$$\hat{H} = g_e\beta \mathbf{B}\,\mathbf{S} + D[Sz^2 - (35/12) + (E/D)(Sx^2 - Sy^2)] + \mathbf{SAI} \qquad (2)$$

where $g_e = 2.0023$ and D and E are the axial and rhombic zero-field splitting parameters respectively [20,37]. For $D \gg h\upsilon = 0.314\ cm^{-1} = 3400$ G, the EPR spectrum is not sensitive to the particular D-value [37]. Thus in the case of Mn^{IV} a D value of 4.0 cm^{-1} was used [38]. Numerical simulation of the Mn^{II} spectrum, shows that the zero field splitting parameter D is 200 G, with $A_{iso} = 107$ G and almost axial ratio $E/D = 0.013$ listed in Table 2.

Table 2
Spin Hamiltonian parameters used for simulation of the Mn^{II} ($S = 5/2$, $I = 5/2$) and Mn^{IV} ($S = 3/2$, $I = 5/2$) EPR spectra for **$Mn^{II}L(OAC)_2$** catalyst.

	D (G)	E/D	A_{iso} (G)
Mn^{II}($S = 5/2$, $I = 5/2$)			
$Mn^{II}L(OAC)_2$	200	0.013 ± 0.005	107
	D (cm^{-1})	E/D	A_{iso} (G)
Mn^{IV} ($S = 3/2$, $I = 5/2$)			
$Mn^{IV}L(OAC)_2$-conformer-1 (65%)	4.0 ± 0.3	0.21 ± 0.005	110
$Mn^{IV}L(OAC)_2$-conformer-2 (35%)	4.0 ± 0.3	0.23 ± 0.005	110

Numerical simulation of the Mn^{IV} ($S = 3/2$, $I = 5/2$) spectrum (Fig. 7A red line) revealed that consists of two Mn^{IV} conformations with slightly different E/D ratios $E/D = 0.21$ and $E/D = 0.23$. A_{iso} was 110 G for both species. These two sets of E/D parameters indicate that there are two Mn^{IV} ($S = 3/2$, $I = 5/2$) conformers differing somehow in the ligand field symmetry. The best simulation was achieved by assuming 65% of conformer-1 with $E/D = 0.21$ and 35% of conformer-2 with $E/D = 0.23$. In Table 2 the simulation parameters for Mn^{II} and Mn^{IV} spectra are listed.

The time evolution of the Mn^{II} and Mn^{IV} species in Fig. 7C shows that under the condition of the experiment described in Fig. 7, the majority of the Mn centers are oxidized from the Mn^{II} to Mn^{IV} state within 20 min, and then the high oxidation states decline to EPR silent states.

$Fe^{II}L(OAC)_2$: Fig. 8A (i) presents the EPR spectrum for $Fe^{II}L(OAC)_2$ powder i.e. with no addition of solvent. The absence of signals shows the absence of Fe^{III}, indicating that all Fe centers are in the ferrous state (Fe^{II}) [20]. After addition of solvent and H_2O_2 (Fig. 8A), a High Spin Fe^{III} ($S = 5/2$) signal was progressively formed, and maximized within ~10 min, see plot of time evolution in Fig. 8C. In parallel, an EPR signal corresponding to Low spin Fe^{III} ($S = 1/2$) was developed. This LS signal was maximized after 20 min and then declined to zero within 30 min Fig. 8A and C.

Numerical calculations of EPR spectra for Fe^{III} ($S = 5/2$) were performed using the spin Hamiltonian

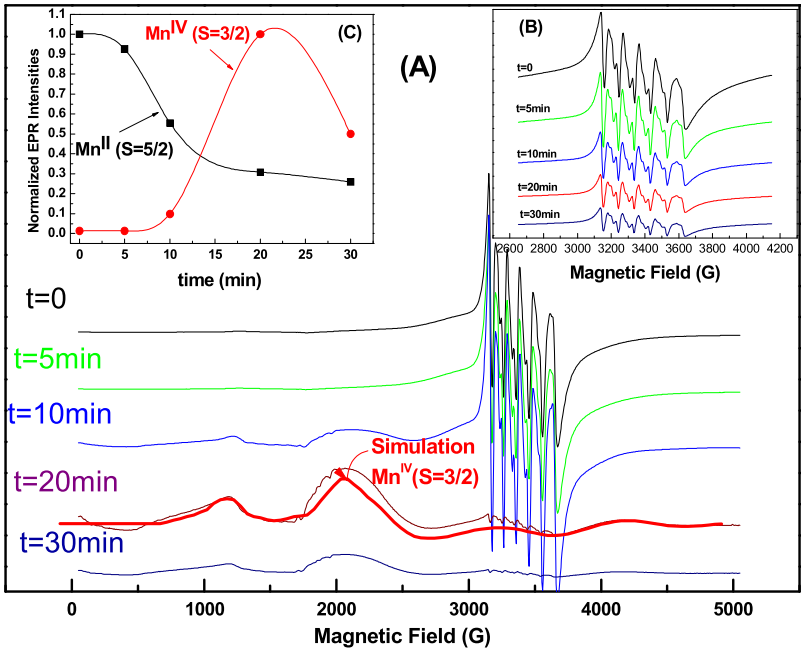

Fig. 7. EPR spectra for **$Mn^{II}L(OAC)_2$** in methanol/acetone: (A) for reaction times $t = 5$, 10, 20, 30 min after addition of CH_3COONH_4 and H_2O_2 (Red line) theoretical Mn^{IV} ($S = 3/2$) EPR spectrum obtained using the spin-Hamiltonian parameters listed in Table 2, (B) same as in (A) zoomed in the Mn^{II} signals and (C) time evolution of Mn^{II} and Mn^{IV} species.

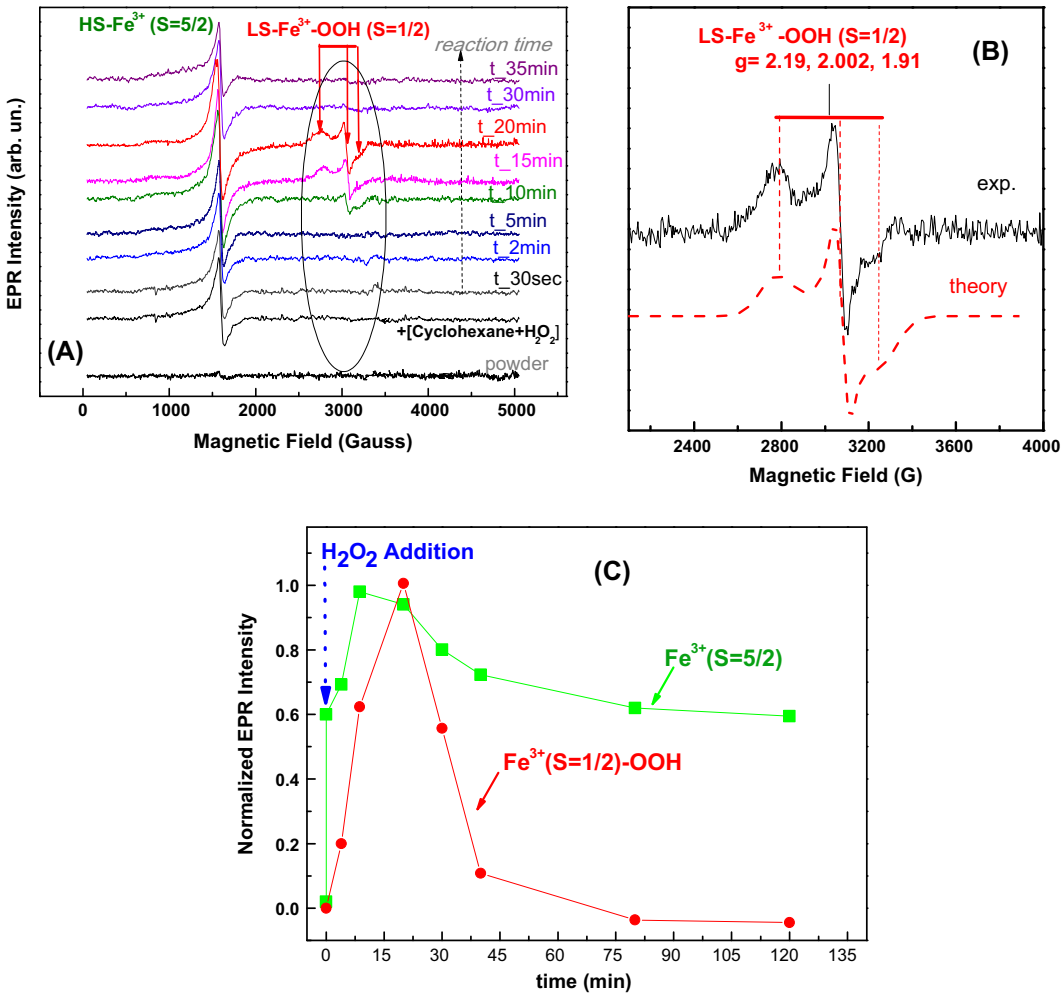

Fig. 8. (A) EPR spectra for $\mathbf{Fe^{II}L(OAC)_2}$ in CH_3CN:powder, after addition of H_2O_2 and substrate, at reaction times t = 5–35 min, (B) a Low-Spin Fe^{III} (S = 1/2) experimental and simulation (red line). Simulations were obtained using the spin-Hamiltonian parameters listed in Table 3 and (C) time evolution of the Fe species.

$$\widehat{H} = g_e\beta \mathbf{B}\,\mathbf{S} + D[Sz^2 - (35/12) + (E/D)(Sx^2 - Sy^2)] \quad (3)$$

where g_e = 2.0023 and D and E are the axial and rhombic zero-field splitting parameters respectively [20,37]. A D value of 3.0 cm^{-1} used, indicative of any $D \gg h\upsilon$ = 0.314 cm^{-1} that is typical of high spin Fe-complexes [37]. The g-values detected in the experimental spectrum are effective g-values resulting from the effect of D and E on the energy levels.

In the case of the Low-Spin Fe^{III} (S = 1/2) we used a simple Zeeman Hamiltonian, with the **g** tensor having principal values the experimental g_1, g_2, g_3 listed in Table 3.

$$\widehat{H} = \beta \mathbf{BgS} \quad (4)$$

Table 3
Spin Hamiltonian parameters used for simulation of the Fe^{III} (S = 5/2) and Fe^{III} (S = 1/2) EPR spectra for $\mathbf{Fe^{II}L(OAC)_2}$ catalyst.

D (cm^{-1})				E/D
High spin Fe^{III} (S = 5/2)				
3.0				0.30
g_1	g_2	g_3	Δ/λ	V/Δ
Low spin Fe^{III} (S = 1/2)				
2.19	2.005	1.91	7.6	0.7

Error bars in g values ±0.05.

Detailed microwave-power dependence study of the low-spin Fe^{3+} signal allowed the identification of the g-tensor components, see Fig. S1 in Supporting Information.

The rhombicity (V/Δ) and tetragonality (Δ/λ) parameters were calculated from the g values [39]. The structural significance of these values can be parametrized by the so-called Peisach-Blumberg diagram i.e. a plot of [V/Δ] vs. [Δ/λ] parameters, Fig. S2 in Supporting Information. Fig. S2 shows that the [V/Δ] vs. [Δ/λ] parameters can vary among heme or non-heme Fe—OOH systems, indicating a high sensitivity to ligand-filed effects. On the other hand the [V/Δ] vs. [Δ/λ] for our LS-LFe^{III} complex falls between those of heme- and non-heme Fe-complexes. We consider that this reflects the "semi-heme" structure of the ligand **L**. Overall, the g-values, [V/Δ] vs. [Δ/λ] parameters, the transient kinetics of the LS-EPR signal (together with the UV–vis spectra) corroborate its assignment to a LS-Fe$^{(III)}$—OOH state characteristic for Low-Spin non-heme ferric complexes where the Fe atom is coordinated by one hydroperoxo-unit [40–42]. From Fig. 8 we observe that [i] the development of Low-Spin L**Fe**^{III}—OOH state follows the oxidative evolution of the High-Spin Fe^{3+} after a time-lapse i.e. indicating that structural rearrangement events occur during this time – not redox advancement- that result in the Low-Spin L**Fe**^{III}—OOH configuration. Typically, formation of a Low-Spin sate is indicative of a strong-ligand field around the iron center. [ii] then, after this Low-Spin L**Fe**^{III}—OOH formation, its decline indicates formation of higher Fe oxidation states [15,41,42], not detected in our EPR

experiments probably due to very short lifetime, a typical case for these highly reactive species [15,41,42]. We underline that, quantitation of the formed LS L**Fe**^{III}—OOH centers indicates that only ~30% of the total Fe is converted from the High-Spin state to the LS L**Fe**^{III}—OOH by H_2O_2. In contrast, H_2O_2 oxidizes almost 100% of the Mn^{II} to Mn^{IV}. Thus the present EPR data reveal a second fundamental difference between $Fe^{II}L(OAC)_2$ and $Mn^{II}L(OAC)_2$:

[% of oxidizable Mn in $MnL(OAC)_2$]
≫ [% of oxidizable Fe in $FeL(OAC)_2$]

This phenomenon, together with the trends in TONs, TOFs, indicates the existence of different thermodynamic barriers that differentiate the catalytic evolution of $Mn^{II}L(OAC)_2$ *vs.* $Fe^{II}L(OAC)_2$. Under comparable solution potentials i.e. ~430 mV in $Mn^{II}L(OAC)_2$ and ~470 mV in $Fe^{II}L(OAC)_2$, the same oxidant H_2O_2 is *less* efficient in Fe advancement at higher oxidation states. This indicates that the $Fe^{II}L(OAC)_2$ catalyst will perform less catalytic turnovers, as we show herein with the catalytic results, and thus will be less efficient in catalysis, in agreement with the present catalytic data in Fig. 4B and Table 1. To obtain numerical values of the thermodynamic barriers, we have monitored the redox/catalytic kinetics of $Mn^{II}L(OAC)_2$ *vs.* $Fe^{II}L(OAC)_2$ *in situ* using low-temperature UV–vis spectroscopy, as we analyze hereafter.

3.2.2. Monitoring the redox/catalytic kinetics by low temperature UV–vis spectroscopy

[$Mn^{II}L(OAc)_2$]: The catalytic reaction for [$Mn^{II}L(OAc)_2$] was monitored in an [acetone: methanol] for a temperatures T = 0 °C to −30 °C. Characteristic time-evolution of the spectra is displayed in Fig. 9A (T = −30 °C) and 9B (T = −15 °C).

Before addition of oxidant, this complex shows a characteristic band at λ_{max} = 420 nm characteristic of the Mn^{II} state [43,44]. After addition of H_2O_2, the spectrum evolves, and a characteristic feature at λ_{max} = 397 nm characteristic of a Mn^{IV}=O species [43,44] is emerging. The formation of this Mn^{IV}=O species is in agreement with our EPR data, Fig. 7.

Thermodynamic parameters E_a, $\Delta H^{\ddagger}$, $\Delta S^{\ddagger}$: The time-evolution of the intensity of the $Mn^{(IV)}$=O band at 397 nm (I_{397}) is plotted in Fig. 10(A) for T = 0, −15, −20, −30 °C respectively. At lower T, less Mn centers achieve oxidation to the Mn^{IV} state; thus at −30 °C, I_{397} is ~50% of that at 0 °C. The Mn^{IV}=O formation kinetics in Fig. 10A shows a strong temperature dependence, revealing the existence of an activation energy barrier. An Arrhenius plot, derived by plotting the [initial kinetic rates (k)], i.e. estimated by the slope of the initial part of the kinetic data, in Fig. 10A *vs.* [1/T] is displayed Fig. 10B. According to the Arrhenius theory [45] the temperature dependence of k provides the energetic characteristic of the catalytic system [45],

$$\ln(k) = (-E_a/R) * (1/T) + C \quad (5)$$

where E_a is the activation energy of the reaction in J/mole, T is the temperature in K, R is the gas constant 8.314 J/K mol and C is a constant to be defined by the fit to the experimental data. In a ln(k) *vs.* (1/T) plot, the Arrhenius process is reflected as a line with slope ($-E_a/R$). Using equation [5], the best-linear fit, (solid line in Fig. 10B), provides an estimate of the activation energy E_a = 58.6 ± 3 kJ/mol, listed in Table 4. This activation barrier corresponds to oxidation of Mn^{II} to Mn^{IV}=O i.e. according to EPR data.

Further analysis of the kinetic rates, using the Eyring-Polani Eq. (6) can provide the enthalpy $\Delta H^{\ddagger}$ and entropy $\Delta S^{\ddagger}$ of the reaction [45]

$$\ln\frac{k}{T} = -\frac{\Delta H^{\ddagger}}{R}\frac{1}{T} + \ln\frac{k_B}{h} + \frac{\Delta S^{\ddagger}}{R} \quad (6)$$

where R is the gas constant = 8.314 J/K mol, T is the absolute temperature, h is the Planck constant = 6.626×10^{-34} J s, and k_B the Boltzmann constant $k_B = 1.380 \times 10^{-23}$ J/K. According to Eq. (6), an Eyring-Polanyi plot, [ln(k/T) *vs.* 1/T], see Fig. 10C, provides a line whose slope equals $-\Delta H^{\ddagger}/T$ and the y-intercept provides $\Delta S^{\ddagger}/R + \ln(k_B/h)$. Accordingly, from the data in Fig. 8C we estimate $\Delta H^{\ddagger}$ = −55.0 ± 3.0 kJ/mole and $\Delta S^{\ddagger}$ = +0.3 ± 0.05 kJ/K mole, listed in Table 4.

[$Fe^{II}L(OAc)_2$]: An analogous thermodynamic analysis, was performed by low-temperature UV–vis experiments were performed at different temperatures for [$Fe^{II}L(OAc)_2$]. Starting with the Fe^{II} complex in CH_3CN, with no oxidant added, bands at 461 and 503 nm were observed at all temperatures, see Fig. 11A and B. After addition of H_2O_2 a new band with a maximum at 420 nm was progressively developed. This new band is characteristic for a Fe^{III}—OOH species formation [40,46–48]. This is the Low-Spin HOO-Fe^{III} (S = 1/2) intermediate detected by EPR, see Fig. 8A and B. More specifically Beller et al. [40] show the formation of Fe-OOH species with absorbance peak at 465 nm. In reference [49] Que et al. demonstrated that the configuration of the "O—O(H)" axial ligation can –in certain cases- be distinguished by the UV–vis band-position in LS-Fe^{3+} O—O(H) [49]. Chiraldi et al. reported that heme pyridine iron complex upon oxidation with H_2O_2 forms a band at 418 nm attributed to the $Fe^{(III)}$—OOH species. In a previous work of our group [50], using a LFe^{III} complex were L = [3-{2—[2-(3-hydroxy-1,3-diphenyl-allylideneamino)-ethyl amino]}-1,3-diphenyl-propen-1-ol] the formation of Fe—OOH was studied by UV–vis. In this study, after the addition of H_2O_2 a band at 413 nm, attributed to $Fe^{(III)}$—OOH, progressively increased.

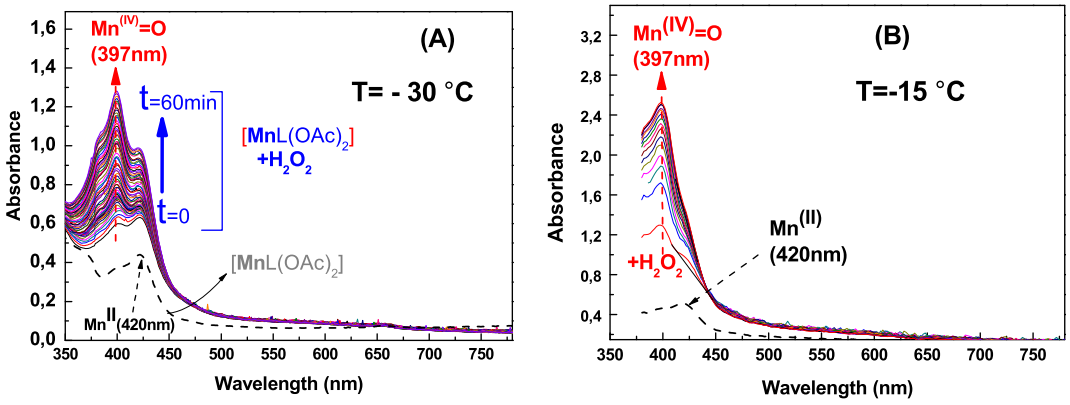

Fig. 9. UV–vis spectra of redox/catalytic kinetics for [**$Mn^{II}L(OAc)_2$**] in [acetone: methanol] (A) reaction temperature −30 °C and (B) reaction temperature −15 °C. Each spectrum has been recorded within 60 s.

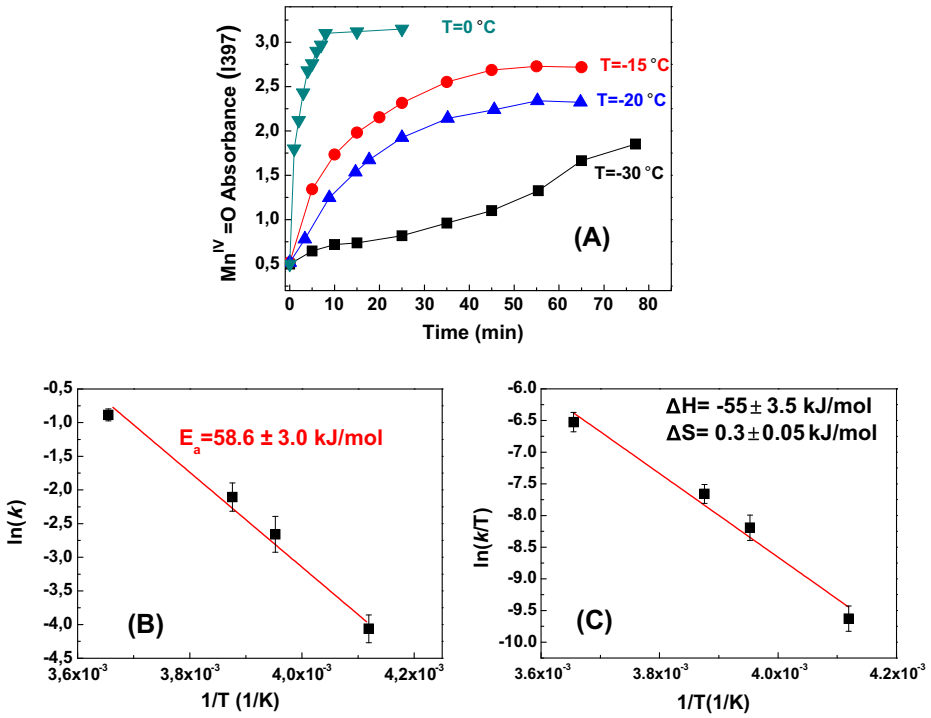

Fig. 10. (A) Kinetics of the of Mn^{IV}=O formation by [$\mathbf{Mn^{II}L(OAc)_2}$], monitored by the I_{397} at different temperatures, (B) Arrhenius plot and (C) Eyring-Polanyi plot of the formation of Mn^{IV}.

Table 4
Thermodynamic parameters estimated for the reaction catalyzed by $\mathbf{Mn^{II}L(OAc)_2}$ and $\mathbf{Fe^{II}L(OAc)_2}$.

	E_a (kJ/mol)	ΔH (kJ/mol)	ΔS (kJ/K mol)	$\Delta G_{(T\text{-}302K)}$ (kJ/mol)
$Mn^{II}L(OAc)_2$	+58.6 ± 3.0	−55.0 ± 3.0	+0.3 ± 0.05	−146 ± 6.0
$Fe^{II}L(OAc)_2$	+91.3 ± 3.0	−84.3 ± 3.0	+0.2 ± 0.05	−144 ± 6.0

The UV–vis spectrum shows also the transient character of the Fe^{3+}—OOH species. At T = +5 °C, see Fig. S3 in Supporting Information the band at 420 nm, due to LFe^{3+}—OOH, is maximized within 10 min, and then it decays rapidly within the next 10 min.

Fig. 12A, shows the kinetic evolution of the Fe^{III}—OOH band at 420 nm (I_{420}) at different temperatures. The Arrhenius and Eyring-Polanyi plots are presented in Fig. 12B and C respectively. Notice that, the kinetic rate of Fe^{II} to Fe^{III}—OOH oxidation is much slower than the Mn^{II} to Mn^{IV} kinetics, is agreement with the TOFs. Under the same redox conditions, higher temperatures i.e. +5 to −5 °C, had to be selected for the iron complex to achieve analogous rates as for Mn complexes i.e. 0 °C to −30 °C, compare Figs. 10A *vs.* 12A. This reveals, that the iron catalyst $Fe^{II}L(OAc)_2$ has to overcome a considerably higher thermodynamic barrier than the $Mn^{II}L(OAc)_2$ catalyst.

Quantitatively, the Arrhenius activation energy is estimated to be E_a = 91.3 ± 3.0 kJ/mol, and $\Delta H^{\ddagger}$ = −84.3 ± 3.0 kJ/mole, $\Delta S^{\ddagger}$ = +0.2 ± 0.05 kJ/K mole, listed in Table 4. At room temperature, T = 302 K, the free energy change for this reaction is $\Delta G^{\ddagger} = \Delta H^{\ddagger} - T\Delta S^{\ddagger}$ = −84−60 = −144 ± 6 kJ/mole.

4. Discussion

The thermodynamic events: Overall, the present thermodymanic data in Table 4 show that

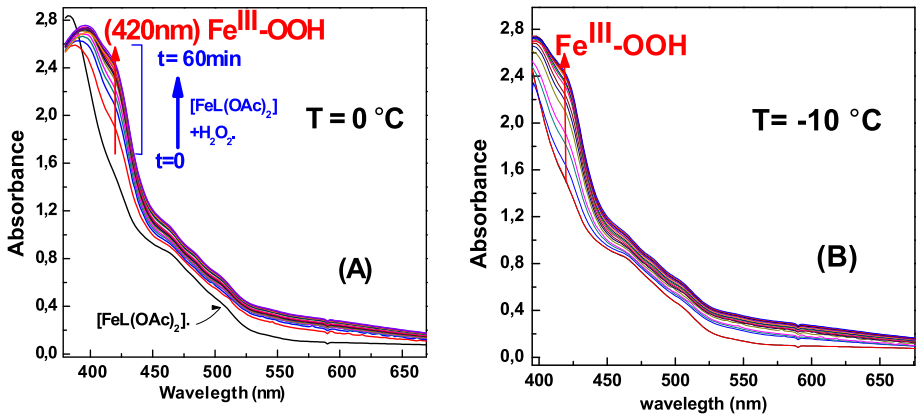

Fig. 11. UV–vis spectra of redox/catalytic kinetics for [$\mathbf{Fe^{II}L(OAc)_2}$] in [CH_3CN] (A) reaction temperature 0 °C and (B) reaction temperature −10 °C. Each spectrum has been recorded within 60 s.

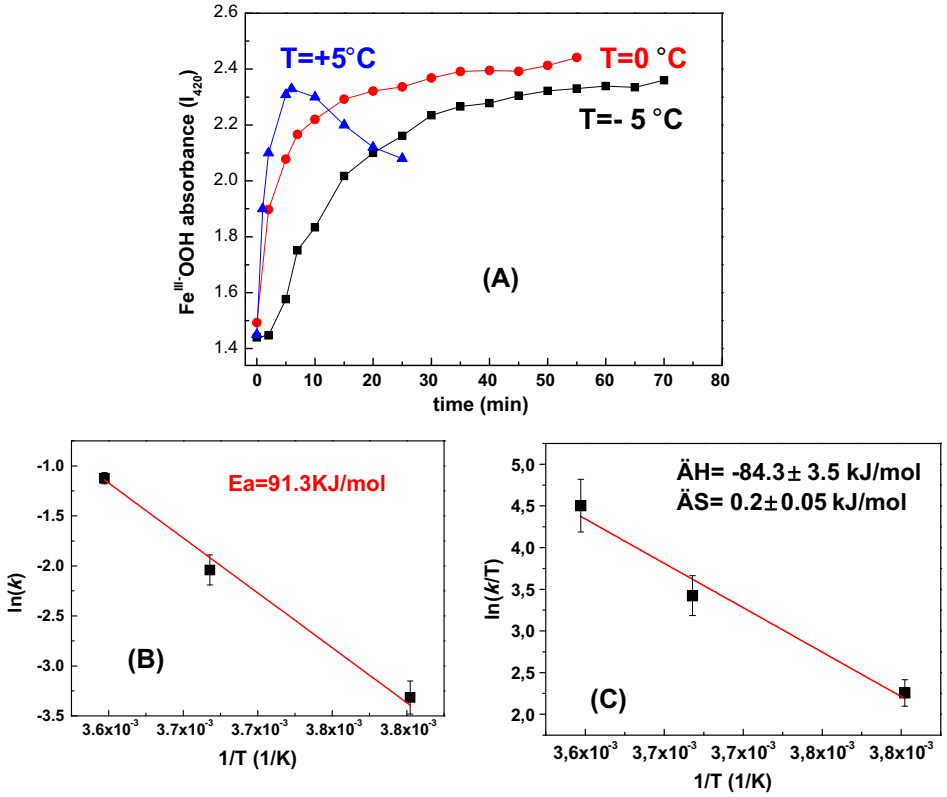

Fig. 12. (A) Kinetics of the of Fe^{III}—OOH formation by $[Fe^{II}L(OAc)_2]$, monitored by the I_{420} at different temperatures, (B) Arrhenius plot and (C) Eyring-Polanyi plot of the formation of Fe^{III}—OOH.

(i) The oxidative advancements of LMn^{II} to LMn^{IV}=O as well as the LFe^{II} to LFe^{III}—OOH are strongly exothermic reactions. At room temperature, $T = 302$ K, where typically our catalytic reactions are performed, the entropic term is $T\Delta S^{\ddagger} = 302 \times 0.3 \sim 91$ kJ/mole; thus, the free energy change for this reaction is $\Delta G^{\ddagger} = \Delta H^{\ddagger} - T\Delta S^{\ddagger} = -55 - 91 = -146 \pm 6$ kJ/mole for $[Mn^{II}L(OAc)_2]$, while $\Delta Gv = \Delta H^{\ddagger} - T\Delta S^{\ddagger} = -144 \pm 6$ kJ/mole for $[Fe^{II}L(OAc)_2]$. Thus we see that in *thermodynamic equilibrium* terms, the overall evolution of $[Mn^{II}L(OAc)_2]$, has only slightly more negative ΔG than the $[Fe^{II}L(OAc)_2]$. This difference is not sufficient to explain the huge differences observed in the TONs of the $[Mn^{II}L(OAc)_2]$ *vs.* the $[Fe^{II}L(OAc)_2]$ catalyst.

(ii) Going to the *kinetics*, i.e. describing the events during the out-of-equilibrium transient states, the activation energy barrier E_a for the oxidative advancement of LMn^{II} to LMn^{IV}=O is $E_a = 58.6 \pm 3.0$ kJ/mol while E_a for LFe^{II} to LFe^{III}—OOH is $E_a = 91.3 \pm 3.0$ kJ/mol. Thus the thermodynamic data in Table 4 reveal that the oxidative advancement of the Fe-catalyst faces a significantly higher activation barrier than the Mn-catalyst

$$E_{a(\mathbf{LFe}(OAC)2)} \gg E_{a(\mathbf{LMn}(OAC)2)}$$

while the free-energy difference

$$\Delta G^{\ddagger}_{(\mathbf{LFe}(OAC)2)} \sim \Delta G^{\ddagger}_{(\mathbf{LMn}(OAC)2)}$$

is comparable in the Fe and Mn complexes. This thermodynamic information can be visualized in Scheme 1.

Taken altogether the present data clarify that the main thermodynamic barrier, ultimately determining the overall catalytic performance, TONs/TOFs, of these homologous Mn and Fe catalysts is the activation energy for the *transient intermediates* i.e. Mn^{II} to Mn^{IV}=O for the $Mn^{II}L(OAC)_2$ and Fe^{II} to Fe^{III}—OOH for the $Fe^{II}L(OAC)_2$. On the other hand the *equilibrium* parameters $\Delta G^{\ddagger}$, $\Delta H^{\ddagger}$, $\Delta S^{\ddagger}$, characteristic for the initial *vs.* final state, do not differ neither in enthalpic nor entropic terms. This shows that molecular reorganization events between initial *vs.* final states have the same energy cost in both $Mn^{II}L(OAC)_2$ and $Fe^{II}L(OAC)_2$ catalysts. From the redox-chemistry point of view i.e. using the fundamental equation $\Delta G^{\ddagger} = -n\ FE_{1/2}$, with $E_{1/2}$ = redox potential of the equilibrium redox states, the comparable $\Delta G^{\ddagger}_{(\mathbf{LFe}(OAC)2)} \sim \Delta G^{\ddagger}_{(\mathbf{LMn}(OAC)2)}$ implies $E_{1/2(\mathbf{LFe}(OAC)2)} \sim E_{1/2(\mathbf{LMn}(OAC)2)}$. Thus the redox potential between the initial/final equilibrium states does not differentiate the Mn- vs the Fe-complex. Instead the activation energy of the transient intermediates is the parameters that makes the observed difference in catalytic reaction rates.

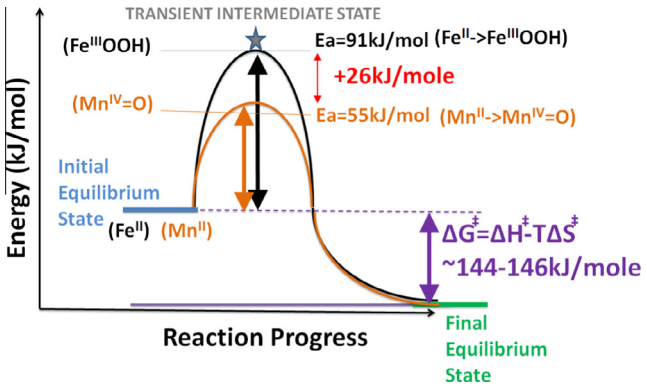

Scheme 1. Comparative thermodynamic reaction scheme for the oxidative evolution of $\mathbf{Mn^{II}L(OAC)_2}$ and $\mathbf{Fe^{II}L(OAC)_2}$ catalysts, according to the data of Table 4. The activation barrier is significantly higher for the Fe-complex than for the Mn-complex, while the total free energy changes $\Delta G^{\ddagger}$ are comparable.

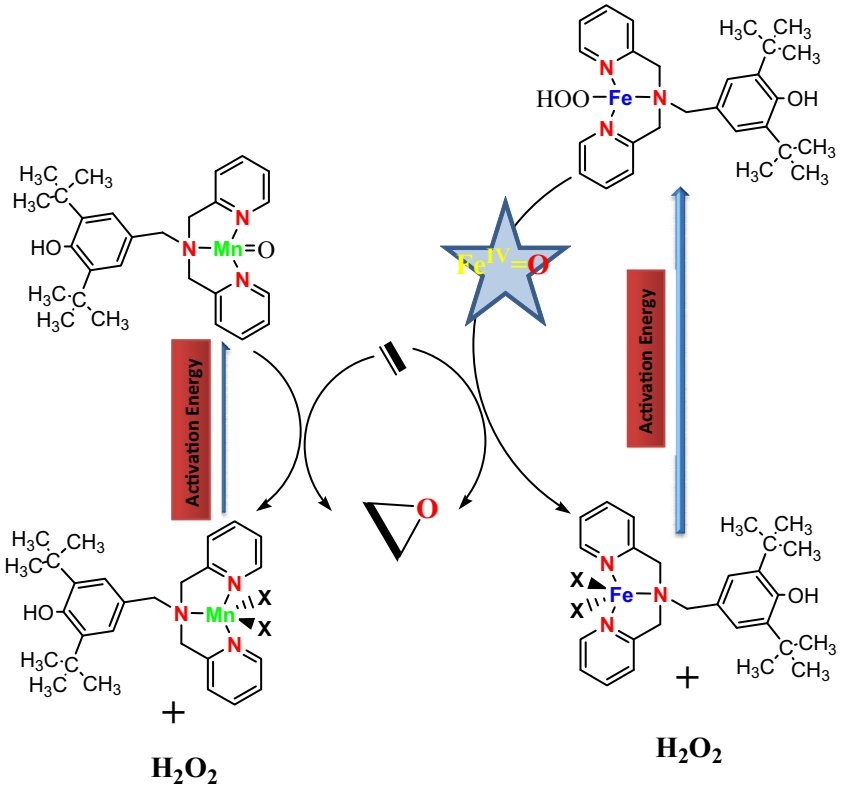

Scheme 2. Catalytic reaction scheme for the oxidative evolution of $\mathbf{Mn^{II}L(OAC)_2}$ and $\mathbf{Fe^{II}L(OAC)_2}$ catalysts, according to our data presented herein.

A unified catalytic reaction mechanism: The thermodynamic reaction scheme when incorporated to a pertinent catalytic cycle, see Scheme 2, provides a unified physicochemical landscape as follows.

Addition of H_2O_2 in Mn^{II}-catalysts produces Mn^{II}—OOH that rapidly oxidizes Mn^{II} to Mn^{IV} i.e. via a two-electron oxidation step [27]. In contrast, Fe^{II} is first oxidized to the intermediate low-spin Fe^{III}—OOH state that further evolves to Fe^{IV}=O [24]. Here it is instructive to underline that, according to our EPR data, only the Low-Spin Fe centers are catalytically active. As shown in Fig. 8B the High-Spin-Fe complexes i.e. those Fe-complexes that fail to be converted to the Low-Spin Fe^{III}—OOH state do evolve also, however at much slower rates than the low-spin states. This superiority of the Low-Spin *vs.* the High-Spin reaction path has been reported previously for other non-heme [24] or heme [15,17] Fe-catalysts also. Thus, in the case of the Fe-catalyst, practically the catalytic activity is determined by the Low-Spin path, as shown herein.

Molecular catalytic events: Given that the catalytic profile of the present iron catalysts is analogous to the non-heme-Fe (DPEIFe^{III}Cl) explored by us recently [24], we consider that the catalytic oxidation mechanism should be similar one i.e. including not only Fe^{IV}=O species but also ·OH formed by a homolytic cleavage of Fe^{III}-hydroperoxides [24]. Electrophilic attack of Fe^{IV}=O species toward alkene could generate a radical [Fe-O-substrate] adduct which subsequently, by intramolecular attack, may liberate epoxides as oxidation products. Detection of allylic oxidation products indicates a first substrate attack by ·OH radicals followed by Fe^{IV}=O association. The Fe^{II} formed during catalysis is re-oxidized by H_2O_2 [24].

On the other hand, the present Mn^{II} catalysts operate exclusively via a 2-electron step forming Mn^{IV}=O which is detected by both EPR and low temperature UV–vis. However, a key-parameter here is ammonium acetate which assists -as additive-acting in two steps [27] (i) by deprotonating H_2O_2 thus promoting readily Mn^{II}—OOH and (ii) by enhancing heterolytic cleavage of Mn^{II}—OOH toward the determinant Mn^{IV}=O formation [27].

For completeness, we reiterate that as shown many times by our group [14–18] ammonium acetate has no effect on Fe-catalysts. Ammonium acetate drives Mn-catalysis quickly and directly to Mn^{IV}=O i.e. Mn^{II}—OOH is *not* the rate-limiting intermediate but rather the Mn^{IV}=O state. This is of great importance in oxidation catalysis, because the generation of the unique Mn^{IV}=O oxidation intermediate in conjunction with its low activation barrier is responsible for the *selective* catalytic epoxidation of alkenes with *high TONs* values observed herein and in analogous Mn^{II}-catalysts.

5. Conclusion

Two sets of homologous Fe and Mn catalysts systematic [Fe^{II}L$(Cl)_2$], [Mn^{II}L$(Cl)_2$], [Fe^{II}L$(OAc)_2$], [Mn^{II}L$(OAc)_2$] have been synthesized. A detailed comparative study of their catalytic oxidative performance in tandem with EPR and Low-Temperature UV–vis has been carried out. It is found that the Mn-catalysts consistently outcompeted the homologous Fe-catalysts i.e. TOFs (Mn) = 162 *vs.* TOFs (Fe) = 16. The Fe-catalysts face a significantly higher activation barrier than the Mn-catalysts i.e. $E_a(\mathbf{Fe^{II}L}(OAC)_2) = 91.3$ kJ/mol $\gg E_a(\mathbf{Mn^{II}L}(OAC)_2) = 58.6$ kJ/mole, while the free-energy difference $\Delta G^{\ddagger}(\mathbf{Fe^{II}L}(OAC)_2) \sim \Delta G^{\ddagger}(\mathbf{Mn^{II}L}(OAC)_2) \sim -145$ kJ/mole did not make difference. A unified/consistent catalytic reaction mechanism is discussed. We suggest that these mechanistic findings bear immediate relevance to the catalytic performance of other analogous non-heme Fe- *vs.* Mn-complexes. Taken altogether the present data clarify that the main thermodynamic barrier, ultimately determining the overall catalytic performance of these homologous Mn- and Fe-catalysts is the activation energy for the *transient intermediates* i.e. Mn^{II} to Mn^{IV}=O for the Mn-catalysts and Fe^{II} to Fe^{III}—OOH for the Fe-catalysts.

Acknowledgments

This work was partially supported by the Russian Foundation for Basic Research (grant no. 15-03-03057).

Appendix A. Supplementary material

Supplementary data associated with this article can be found, in the online version, at http://dx.doi.org/10.1016/j.jcat.2016.06.017.

References

[1] R.A. Sheldon, Top. Curr. Chem. 164 (1993) 21.
[2] K.A. Jorgenson, Chem. Rev. 89 (1989) 431–458.
[3] M. Islam, P. Mondal, S. Mokherjee, M. Mobarak, A.S. Roy, S. Mondal, S. Sarkar, J. Chem. Technol. Biotechnol. 85 (2010) 460–470.
[4] C.L. Hill, C.M. Prosser-McCartha, Coord. Chem. Rev. 143 (1995) 407–455.
[5] K. Sato, M. Aoki, R. Noyori, Science 281 (1998) 1646–1647.
[6] E.J. Larson, V.L. Pecoraro, in: V.L. Pecoraro (Ed.), Manganese Redox Enzymes, Verlag-Chemie, New York, 1992, p. 1.
[7] B. Meunier, Biomimetic Oxidations Catalyzed by Transition Metal Complexes, Imperial College Press, London, 2000.
[8] A. Berkessel, M. Franenkron, T. Schwenkreis, A. Steinwetz, J. Mol. Catal A – Chem. 117 (1997) 339.
[9] J. Bjernemose, A. Hazell, C.J. McKenzie, M.F. Mahon, L.P. Nielsen, P.R. Raithby, O. Simonsen, H. Toftlund, J.A. Wolny, Polyhedron 22 (2003) 875–885.
[10] J.P. Wikstrom, A.Y. Nazarenko, W.M. Reiff, E.V. Rybak-Akimova, Inorg. Chim. Acta 360 (2007) 3733–3740.
[11] W.A. Chomitz, S.G. Manasian, A.D. Sutton, J. Arnold, Inorg. Chem. 46 (2007) 7199–7209.
[12] E.R. Milaeva, Curr. Top. Med. Chem. 11 (2011) 2703–2713.
[13] E.R. Milaeva, O.A. Gerasimova, A.L. Maximov, E.A. Ivanova, E.A. Karachanov, N. Hadjiliadis, M. Louloudi, Catal. Commun. 8 (2007) 2069–2073.
[14] K.C. Christoforidis, M. Louloudi, E.R. Milaeva, Y. Sanakis, Y. Deligiannakis, Mol. Phys. 105 (2007) 2185–2194.
[15] K.C. Christoforidis, M. Louloudi, E.R. Milaeva, Y. Deligiannakis, J. Catal. 270 (2010) 153–162.
[16] K.C. Christoforidis, M. Louloudi, Y. Deligiannakis, Appl. Catal. B: Environ. 95 (2010) 297–302.
[17] K.C. Christoforidis, M. Louloudi, Y. Deligiannakis, Chem. Phys. Lett. 494 (2010) 289–294.
[18] K.C. Christoforidis, E. Serestatidou, M. Louloudi, I.K. Konstantinou, E.R. Milaeva, Y. Deligiannakis, Appl. Catal. B: Environ. 101 (2011) 417–424.
[19] E.R. Milaeva, D.B. Shpakovsky, Y.A. Gracheva, S.I. Orlova, V.V. Maduar, B.N. Tarasevich, N.N. Meleshonkova, L.G. Dubova, E.F. Shevtsova, Dalton Trans. 42 (2013) 6817–6828.
[20] J.R. Pilbrow, Transition Metal Electron Paramagnetic Resonance, Oxford Science Publications, Clarendon Press, Oxford, England, 1991.
[21] W. Adam, C. Mock-Knoblauch, C.R. Saha-MÖller, M. Helderich, J. Am. Chem. Soc. 122 (2000) 9685–9691.
[22] D.P. Kessissoglou, X. Li, W.M. Butler, V.L. Pecoraro, Inorg. Chem. 26 (1987) 2487–2492.
[23] K. Srinivasan, P. Michaud, J.K. Kochi, J. Am. Chem. Soc. 108 (1986) 2309–2320.
[24] G. Bilis, P. Stathi, A. Mavrogiorgou, Y. Deligiannakis, M. Louloudi, Appl. Catal. A: Gen. 470 (2014) 376–389.
[25] S. Hong, K.D. Sutherlin, J. Park, E. Kwon, M.A. Siegler, E. Solomon, W. Nam, Nature Commun. 5 (2014) (ar. no. 5440).
[26] J. Chen, K.-B. Cho, Y.-M. Lee, Y.H. Kwon, W. Nam, Chem. Commun. 51 (2015) 13094–13097.
[27] A. Mavrogiorgou, M. Papastergiou, Y. Deligiannakis, M. Louloudi, J. Mol. Catal. A 393 (2014) 8–17.
[28] S. Stoll, A. Schweiger, J. Magn. Reson. 178 (2006) 42–55.
[29] Ag. Stamatis, Ch. Vartzouma, M. Louloudi, Catal. Commun. 12 (2011) 475–479.
[30] Ag. Stamatis, P. Doutsi, Ch. Vartzouma, K.C. Christoforidis, Y. Deligiannakis, M. Louloudi, J. Mol. Catal. A 297 (2009) 44–53.
[31] G.B. Shul'pin, J. Mol. Catal. A 189 (2002) 39–66.
[32] N.C. Anastasiadis, G. Bilis, J.C. Plakatouras, C.P. Raptopoulou, V. Psycharis, C. Beavers, S.J. Teat, M. Louloudi, S.P. Perlepes, Polyhedron 64 (2013) 189–202.
[33] W. Nam, Acc. Chem. Res. 48 (2015) 2415–2423.
[34] G. Yin, Acc. Chem. Res. 46 (2013) 483–492.
[35] X. Wu, M.S. Seo, K.M. Davis, Y.-M. Lee, J. Chen, K.-B. Cho, H. Yoon, Y.J. Park, S. Fukuzumi, Y.N. Pushkar, W. Nam, J. Am. Chem. Soc. 135 (2013) 6388–6391.
[36] M.J. Camenzind, F.J. Hollander, C.L. Hill, Inorg. Chem. 22 (1983) 3776–3784.
[37] B. Gaffney, H.J. Silverstone, in: L.J. Berliner, J. Reuden (Eds.), Biological Magnetic Resonance, Plenum Press, New York, 1993, pp. 1–57.
[38] C. Duboc, Marie-Noelle Collomb, F. Neese, Appl. Magn. Reson. 37 (2010) 229–245.
[39] C.P.S. Taylor, Bioch. Bioph. Acta 491 (1977) 137–149.
[40] F.G. Gelalcha, G. Anilkumar, M.K. Tse, A. Br Ückner, M. Beller, Chem. Eur. J. 14 (2008) 7687–7698.
[41] L. Duelund, H. Toftlund, Spectrochim. Acta A 26 (2000) 331–340.
[42] K. Chen, M. Costas, J. Kim, A.K. Tripton, L. Que, J. Am. Chem. Soc. 124 (2002) 3026–3035.
[43] R. Giovannetti, in: J. Uddin (Ed.), Macro to Nano Spectroscopy, InTech, 2012, pp. 87–108.
[44] G.G. Martirosyan, A.S. Azizyan, T.S. Kurtikyan, P.C. Fond, Inorg. Chem. 45 (2006) 4079–4087.
[45] K.J. Laidler, Chemical Kinetics, third ed., Harper & Row, New York, 1987.
[46] G. Roelfes, M. Lubben, K. Chen, R.Y.N. Ho, A. Meetsma, S. Genseberger, R.M. Hermant, R. Hage, S.K. Mandal, V.G. Young Jr., Y. Zang, H. Kooijman, A.L. Spek, L. Que Jr., B.L. Feringa, Inorg. Chem. 38 (1999) 1929–1936.
[47] R.A. Ghiladi, K.D. Karlin, Inorg. Chem. 41 (2002) 2400–2407.
[48] G.C. Silva, G.L. Parrilha, N.M.F. Carvahlo, V. Drago, C. Fernandes, A. Horn Jr., O.A. C. Antunes, Catal. Today 133–135 (2008) 684–688.
[49] G. Roefles, V. Vrajmasu, K. Chen, R.Y.N. Ho, J. Rohde, C. Zondervan, R.M. La Crois, E.P. Schudde, M. Lutz, A.L. Spek, R. Hage, B.L. Feringa, E. Munk, L. Que, Inorg. Chem. 42 (2003) 2639–2653.
[50] G. Billis, K.C. Christoforidis, Y. Deligiannakis, M. Louloudi, Catal. Today 157 (2010) 101–106.